548–560 *Nucleic Acids Research, 2020, Vol. 48, No. 2* *Published online 4 December 2019*
doi: 10.1093/nar/gkz1137

Free energy landscape of salt-actuated reconfigurable DNA nanodevices

Ze Shi[1] and Gaurav Arya[2,*]

[1]Department of NanoEngineering, University of California, San Diego, La Jolla, CA 92093, USA and [2]Department of Mechanical Engineering and Materials Science, Duke University, Durham, NC 27708, USA

Received October 05, 2019; Revised November 15, 2019; Editorial Decision November 19, 2019; Accepted December 02, 2019

ABSTRACT

Achieving rapid, noninvasive actuation of DNA structures is critical to expanding the functionality of DNA nanotechnology. A promising actuation approach involves introducing multiple, short pairs of single-stranded DNA overhangs to components of the structure and triggering hybridization or dissociation of the overhangs via changes in solution ionic conditions to drive structural transitions. Here, we reveal the underlying basis of this new approach by computing via molecular simulations the free energy landscape of DNA origami hinges actuated between open and closed states. Our results reveal how the overhangs collectively introduce a sharp free-energy minimum at the closed state and a broad energy barrier between open and closed states and how changes in ionic conditions modulate these features of the landscape to drive actuation towards the open or closed state. We demonstrate the critical role played by hinge confinement in stabilizing the hybridized state of the overhangs and magnifying the energy barrier to dissociation. By analyzing how the distribution of overhangs and their length and sequence modulate the energy landscape, we obtain design rules for tuning the actuation behavior. The molecular insights obtained here should be applicable to a broad range of systems involving DNA hybridization within confined systems.

INTRODUCTION

In DNA nanotechnology, achieving controllable motion is a key step to creating the next generation of dynamic DNA nanodevices (1–7). One strategy for actuating DNA structures involves binding of external biomolecules to reconfigure DNA devices (8–10). A popular method is toehold-mediated strand displacement, where one of the strands in an existing DNA duplex is displaced by an externally provided strand that can form a more stable duplex (11). In this manner, hybridized connections between device components may be released, or reestablished to enable reversible actuation. This method offers the benefits of sequence specificity of displacement strands and ease of introducing displacement sites within devices. However, due to the need for external strands, release of waste strands, and slow kinetics of the displacement reaction, the method can be invasive and slow. Another actuation strategy involves integrating stimuli-responsive molecular entities into the devices, which makes the actuation less invasive and more responsive to environmental stimuli. These entities include base-stacking motifs, DNA triplexes, azobenzene moieties and I-motifs that respond to environmental cues like light, temperature, pH and ions to establish or disrupt interactions between device components (12–16). A third strategy involves using external forces to reconfigure devices. These forces may be applied via electrical or magnetic fields (17,18), via depletants (19), or via optical traps and atomic force microscope tips (20,21). Since the forces are applied directly to the structures and can be modulated fairly rapidly with existing capabilities, these methods can achieve rapid actuation response times, albeit with advanced fabrication and instrumentation requirements.

Recently, we proposed a promising actuation method that combines the noninvasiveness of environmental triggers with the specificity of DNA hybridization to enable rapid reconfiguration of devices with response times comparable to force-based methods (22). The method involves introducing multiple, weakly complementary pairs of single-stranded DNA overhangs to the device components to be actuated, and using changes in solution cation concentration to trigger rapid hybridization or dehybridization of the overhangs to drive conformational transitions in the device. Because this process involves collective hybridization of many short strands, and also does not involve any diffusion of strands or displacement of one hybridized strand with another, this method exhibits much faster response times compared to the strand-displacement method. As demonstration, the method was applied to a DNA origami hinge that nominally exhibits open conformations with its arms subtending large angles about the vertex (Figure 1). By introducing short, complementary overhangs to the inner surfaces of the

*To whom correspondence should be addressed. Tel: +1 919 660 5435; Fax: +1 919 660 8963; Email: gaurav.arya@duke.edu

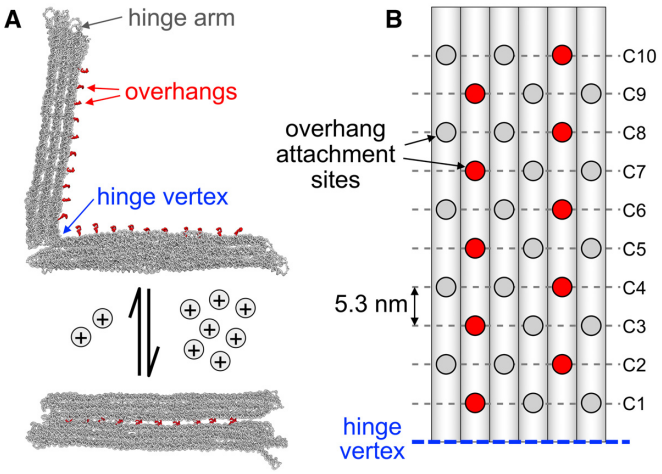

Figure 1. Ion-actuated DNA origami hinge. (**A**) Pairs of complementary single-stranded DNA overhangs introduced into the hinge arms enable them to be reversibly actuated between open (top) and closed (bottom) states via the hybridization or de-hybridization of the overhangs as triggered by changes in cation concentration. (**B**) Schematic showing all available overhang attachment sites (circles) on a hinge arm spread over 10 distances from the vertex, labelled C1 to C10. One possible arrangement of overhangs (red circles) in a 10-connection hinge design is shown.

two hinge arms, the modified hinges could be efficiently actuated between conformations with open and closed arms using a variety of cations, including mono-, di- and trivalent ions. The actuation responses—fraction of hinges exhibiting closed arms versus cation concentration—were characterized as a function of the number and length of overhangs and the bending stiffness of the hinge joint. The results revealed strong, intriguing variations with respect to these design variables, suggesting high tunability of the actuation responses.

Based on our current understanding, the actuation mechanism may be explained as a competition between (i) the intrinsic predisposition of the 'bare' device (minus overhangs) to exhibit open conformations and (ii) the hybridization of overhangs that favors closed conformations. The former effect stems from the underlying structural design of the bare device which dictates intra- and intermolecular interactions between components, and hence their preferred conformations. In DNA hinges, the open conformation appears to arise from the mechanics of the DNA joint connecting the hinge arms, and not from electrostatic repulsion between them, given that the bare hinges exhibited similar hinge-angle distributions across a wide range of cation concentrations. The latter effect provides the driving force necessary for the device to overcome its natural propensity for open conformations and transition to a closed conformation. Importantly, the strength of this driving force depends on cation concentration. At low ion concentrations, the overhangs prefer to remain unhybridized, and the device retains the open conformation it exhibits without overhangs. As ion concentration is raised, the hybridized state of the overhangs becomes increasingly stabilized, causing an increasingly larger fraction of structures to exhibit closed conformations.

In the original study (22), we expressed both these effects in thermodynamic terms, the former in terms of a free energy difference ΔG_{bare} between the open and closed states, and the latter in terms of a hybridization free energy $\Delta G_{\text{hyb}}(c)$ that depends on ion concentration c. Assuming that all overhang pairs are indistinguishable, we formulated a simple, two-state thermodynamic model for the probability of observing closed hinges as a function of ion concentration and the two free energies. Since the hybridization free energy of the tethered, confined overhangs must be distinct from that of free strands in solution, we cast $\Delta G_{\text{hyb}}(c)$ as an additive correction ΔG_{corr} to the *solution*-state hybridization free energy obtained from secondary-structure prediction algorithms. Using the unknowns ΔG_{bare} and ΔG_{corr} as fitting parameters, we were able to obtain good agreement with the experimentally measured actuation responses. While this description was useful for establishing the importance of bare-device mechanics and overhang hybridization in actuation and for fitting experimental data, our knowledge of the actuation mechanism remains very qualitative. For instance, the free energies contributed by the device and the overhangs, and how they vary with the 'reaction coordinate' and ion concentration to 'tilt' the overall free energy towards the open or closed conformations remain unknown. How these free energies change with the various design parameters and the associated molecular mechanisms also are not known. Elucidating these energetic and molecular mechanisms would be crucial to facilitate future design and optimization of actuation devices and responses.

Here, we provide such a quantitative, mechanistic basis of this actuation method through calculation of free energy landscapes via molecular simulations, using the DNA hinge as our model system. Ideally, all-atom simulations should provide the most accurate description of the hinges. However, due to the large system size and slow timescales of hybridization and dissociation, such simulations would require prohibitive computational costs. Hence, we use the coarse-grained model, *oxDNA* (23,24), to represent our hinges. oxDNA has been applied to a variety of DNA nanostructures, (23,25–32) and shown to yield accurate descriptions of their mechanics, conformational dynamics, and ion-dependent hybridization thermodynamics, suggesting that this model should provide reasonable predictions for the ion-actuated DNA hinges studied here. To further alleviate computational costs, we devised a strategy that involves splitting the system into the bare hinge (large structure with short relaxation time) and the different pairs of overhangs (small systems with long relaxation times), and computing their free energies separately using efficient simulation approaches. Consequently, we were able to obtain not only the overall free energies of the overhang-modified DNA hinges as a function of its conformation (hinge angle), but also the free energy contributions arising from the hinge joint and each of the overhang pairs. By computing such energy landscapes for a range of ionic conditions and overhang design parameters, analyzing the conformations of the overhangs, and relating features of the landscape to actuation responses and rates, we were able to provide a more complete, molecular-level understanding of the actuation mechanism that could be used for designing and optimiz-

ing actuation responses. The results obtained here would be important not only for hinge actuation, but many other systems involving DNA hybridization in confined media, including DNA-tethered nanoparticles (33), DNA microarrays (34) and assembly of DNA origami tiles (35).

MATERIALS AND METHODS

We studied here the same DNA origami hinge used earlier to experimentally demonstrate the ion-mediated actuation approach (22). Briefly, the hinge is composed of two stiff arms, each assembled from a 3 × 6 bundle of interconnected double-stranded DNA helices organized in a square lattice. The arms are connected by a linear array of 2 bases- and 16 bases-long single-stranded scaffold connections that form the hinge rotation axis (Figure 1A). Without overhangs, the hinge exhibited mostly open conformations with its arms subtending a broad distribution of angles about a mean angle of ∼80°. To actuate the hinge between such open conformations and a closed conformation, the hinge arms were modified to include short, complementary single-stranded DNA overhangs distributed evenly across the inner face of each arm at reciprocal locations (Figure 1B). Because of the helical structure of DNA and the square-lattice arrangement of DNA helices in the hinge arms, the overhangs could only be introduced at specific locations on the helices lining the inner surface of the arms, which restricted the separation distance between adjacent overhangs on a helix to multiples of 10.6 nm, i.e. the length of 32 bp, or 3 turns of DNA. The experiments explored actuation using 10, 20 and 30 such overhangs per arm (Figure 1B). The overhang pairs were each 7 bases long of sequence ||-TTTCGAC-5′ and 3′-GTCGTTT-||, where '||' denotes hinge arms. Thus, only the terminal four bases contributed to hybridization across the arms, and the inner three bases played the role of flexible linkers. The caDNAno and geometrical designs of the hinges along with a close-up of the hinge joint showing connections between the two arms are provided in Supplementary Figures S1 and S2.

Here, we seek to compute the free energy $G_{\text{hinge}}(\theta)$ of these overhang-modified hinges as a function of the angle θ subtended by the two arms about the hinge joint (vertex) representing the coordinate most descriptive of the conformational transition between the open and closed state. While all-atom molecular dynamics (MD) simulations are the ideal resolution for computing such free energy landscapes, such calculations would entail prohibitive computational costs given the large dimensions of the hinges (∼50 nm), slow timescales of the rotation of hinge arms via Brownian motion (tens of microseconds based on simulations (31) and theory (36,37)), and even longer timescales for the hybridization-dissociation of the overhangs (milliseconds (38)). To this end, we used a coarse-grained model to treat the hinges, namely, the oxDNA model (23,24) in which each nucleotide is modeled as a rigid body with three interaction sites that capture Watson-Crick base-pairing, base stacking, excluded volume, and backbone connectivity. We have shown (31) that this model can accurately capture the conformational dynamics of bare hinges, and others have shown that the model accurately describes the molecular mechanism and thermodynamics of DNA hybridization (23,27,30).

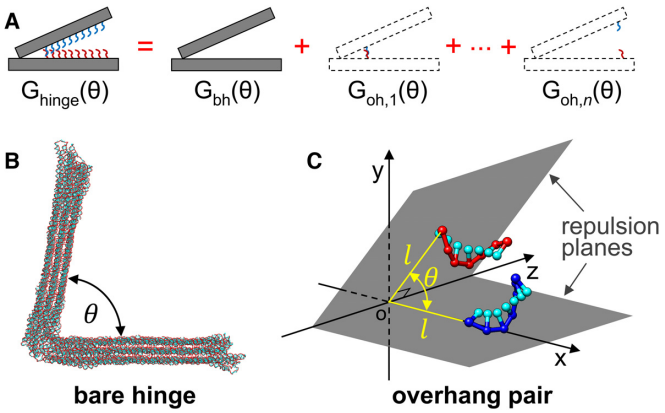

Figure 2. Overall strategy for efficiently computing the free energy landscape of hinge actuation as a function of hinge angle. (**A**) Overhang-modified hinge is split into two parts: the bare hinge and the overhangs. The total free energy $G_{\text{hinge}}(\theta)$ can be written as the sum of the free energy $G_{\text{bh}}(\theta)$ of the bare hinge and the free energies $G_{\text{oh},i}(\theta)$ of the $i = 1, \cdots, n$ pairs of overhangs. (**B**) G_{bh} is computed from MD simulations of the bare hinge. (**C**) $G_{\text{oh},i}$ are computed from VMMC simulations of the overhang pairs using repulsion planes to mimic the confinement of the hinge arms. Phosphate backbones of the two overhangs are shown in red and blue, and all nucleosides are shown in cyan.

In spite of the coarser representation, the computation of $G_{\text{hinge}}(\theta)$ is still highly challenging, as it would require simulations of the entire hinge over timescales longer than their slowest relaxation time, associated with hybridization of overhangs. To tackle this problem, we considered splitting the overall free energy into two contributions, as given by $G_{\text{hinge}}(\theta) = G_{\text{bh}}(\theta) + G_{\text{oh}}(\theta)$ (Figure 2A). The first term is the contribution arising from the bare hinge (without overhangs) that accounts for joint mechanics and intermolecular interactions between the arms. $G_{\text{bh}}(\theta)$ was calculated via the umbrella sampling approach that involved performing a set of harmonically-restrained MD simulations of the bare hinge (Figure 2B) and analyzing the resulting hinge angle distributions using the weighted histogram analysis method (WHAM). The second term is the contribution from all overhangs, including their interactions amongst themselves and with the hinge arms. Based on several assumptions, we were able to divide G_{oh} into independent contributions $G_{\text{oh},\,i}$ from each of the n pairs of overhangs attached at different locations on the arms (Figure 2A), i.e. $G_{\text{oh}}(\theta) = \sum_{i=1}^{n} G_{\text{oh},i}(\theta)$, and also replace the molecularly-detailed hinge arms with simple 'repulsion' planes representing the inner surface of the arms that prevent the phosphate and nucleoside groups of the overhangs from crossing the planes (Figure 2C). This allowed us to use highly efficient virtual-move Monte Carlo (VMMC) simulations for carrying our umbrella sampling of overhang conformations, which together with a modified WHAM approach provided us $G_{\text{oh},i}(\theta)$ as well as free energy contribution $G_{\text{oh},i}(\theta, \xi)$ from the different hybridization states ξ of each overhang pair. See Supplementary Material and associated Supplementary Figures S3–S6 for methodological details of these calculations, a more detailed discussion of the underlying assumptions, and the checks performed to

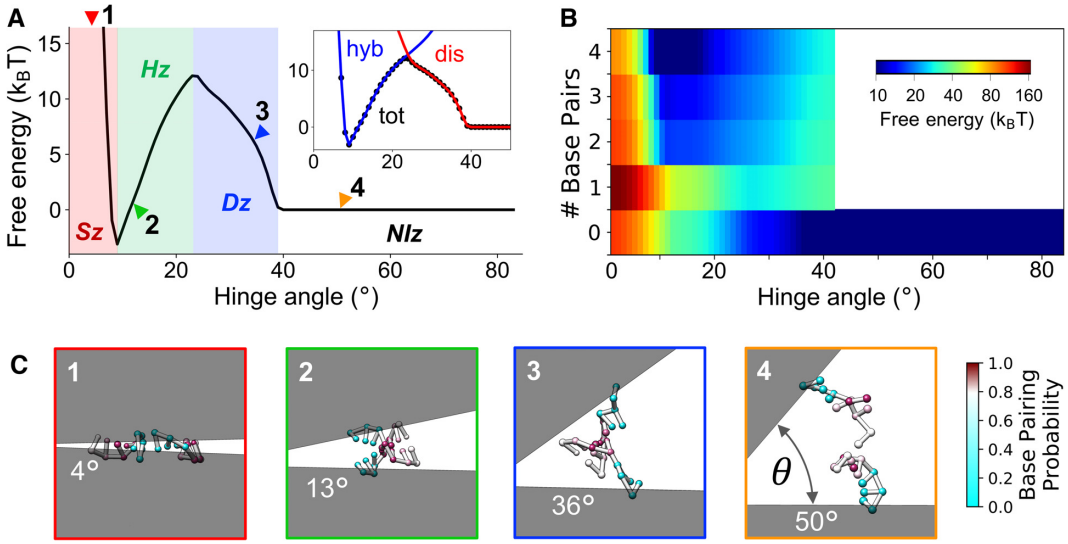

Figure 3. Free energy landscape and conformations of an overhang pair. (**A**) Free energy $G_{\mathrm{oh},i}(\theta)$ for overhangs with four complementary bases and 3-base linkers attached at location C1 and computed at $[Na^+] = 0.2$ M and 300 K. The steric-repulsion (*Sz*), hybridization (*Hz*), dissociation (*Dz*) and non-interaction (*Nlz*) zones are marked by distinct color backgrounds. Inset shows contributions $G_{\mathrm{hyb},i}(\theta)$ (blue) and $G_{\mathrm{dis},i}(\theta)$ (red) to $G_{\mathrm{oh},i}(\theta)$ (circles) from partly- to fully-hybridized states and dissociated states, respectively. (**B**) Free energy contributions $G_{\mathrm{oh},i}(\theta, \xi)$ from the different hybridization states ξ of the overhangs. Empty region in the plot indicates states whose free energies could not be reliably computed due to the extremely low probabilities of occurrence of those states. (**C**) Representative conformations of the overhangs corresponding to angles marked by arrow heads on the energy landscape. Nucleotides are colored as per their base-pairing probability, where cyan means fully dissociated and magenta mostly hybridized states.

ensure adequate sampling of the hinge arms and the overhangs.

The end result of these simplifications is that the prohibitive calculation of $G_{\mathrm{hinge}}(\theta)$ is now reduced to less demanding calculations of $G_{\mathrm{bh}}(\theta)$ and $G_{\mathrm{oh},i}(\theta)$: the calculation of $G_{\mathrm{bh}}(\theta)$ is no longer limited by the long simulation timescales required for sampling the hybridization states of the overhangs, while the $G_{\mathrm{oh},i}(\theta)$ calculations are efficiently able to sample all their hybridization states because of the much smaller system size. Using such an approach, we computed the free energy landscape of the experimental overhang-modified hinges, focusing on contributions from the bare hinge and from each of the overhangs. Unless otherwise stated, we used the overhang sequences specified earlier attached at the 10 different locations on the hinge arms depicted in Figure 1B. To investigate how these overhangs 'close' the hinge arms with increasing ionic strength, we performed simulations at different ion concentrations to elucidate how the energy landscapes are modulated by ionic conditions. Since the oxDNA model has only been parameterized for Na^+ ions, the simulations were performed with 0.2, 0.4 and 1.2 M Na^+ concentrations at 300 K. Lastly, we also investigated the effects of the lengths of the linker and binding portions of the overhangs, two design parameters expected to affect the hybridization energy of overhangs under confinement.

RESULTS

Free energy landscape of the overhangs

In general, the free energy landscape $G_{\mathrm{oh},i}(\theta)$ of the overhang pairs computed at various cation concentrations and tethered at different locations on the hinge arms exhibit a plateau at large hinge angles, a sharp minimum at small angles, and an energy barrier separating the two. Figure 3A presents one such landscape computed at $[Na^+] = 0.2$ M for overhangs tethered at the closest connection point from the hinge vertex (labeled C1 in Figure 1B) that exhibits a free energy gain of $\sim -4k_BT$ at the minimum and a large barrier of $\sim 12k_BT$, relative to the plateau.

To investigate the molecular basis for this characteristic shape of the landscape, we analyzed the free energy contributions $G_{\mathrm{oh},i}(\theta, \xi)$ arising from all possible hybridization states $\xi = 0, 1, \cdots, 4$ of the overhangs, spanning fully dissociated ($\xi = 0$) to fully associated overhangs ($\xi = 4$) (Figure 3B). The five states represent mutually exclusive 'subensembles' of the overall ensemble of overhang conformations, and hence their free energies combine exponentially to yield the overall free energy, that is, $e^{-G_{\mathrm{oh},i}(\theta)/k_BT} = \sum_\xi e^{-G_{\mathrm{oh},i}(\theta,\xi)/k_BT}$. The magnitudes of $G_{\mathrm{oh},i}(\theta, \xi)$ allow us to assess the relative and absolute importance of each hybridization state at various points (hinge angles) along the energy landscape. Also provided are representative conformations of the overhangs captured from simulations at key points along the landscape (Figure 3C).

The following molecular picture of the overhangs emerges from these analyses: At large angles, the overhangs are too far from each other to interact, and the free energy remains flat. The $G_{\mathrm{oh},i}(\theta, \xi)$ map confirms that the overhangs exhibit only the dissociated state ($\xi = 0$) at these large angles (Figure 3B). At $\theta \approx 40°$, the strands begin to interact (configuration 4 in Figure 3C). As the angle decreases further, the strands begin to form unstable base pairs, as noted from the relatively large free energies of the hybridized states ($\xi = 1$–4), which arises from the stretching of the overhangs to form base pairs (configuration 3). Concurrently, the free energy of the dissociated state ($\xi = 0$) begins to rise, evidently from the increasing confinement imposed by the

hinge arms, which leads to increasing entropy loss and electrostatic repulsion between the overhangs. It is this increase in the dissociated-state free energy that is apparently responsible for the observed increase in the overall free energy with decreasing angle. At the peak of the energy barrier, the hybridized and dissociated overhangs exhibit similar free energies and are therefore more or less equally prevalent. At smaller angles, the hybridized states start to become increasingly dominant, with the fully-hybridized state ($\xi = 4$) becoming highly favored at the free energy minimum (configuration 2). Thereafter, the angle becomes severely constricted, and the free energy of all overhang states, both hybridized and dissociated, shoot up due to strong compression of the overhangs by the two arms (configuration 1).

The $G_{\mathrm{oh},i}(\theta, \xi)$ map in Figure 3B shows a visible shift in the population of overhang conformations from dissociated to hybridized states with decreasing angle. This transition can be better captured and related to the shape of the energy landscape by examining the *combined* free energy of all partly- to fully-hybridized states $G_{\mathrm{hyb},i}(\theta) \equiv \sum_{\xi=1}^{4} G_{\mathrm{oh},i}(\theta, \xi)$ along with that of the fully dissociated state $G_{\mathrm{dis},i}(\theta) \equiv G_{\mathrm{oh},i}(\theta, \xi = 0)$, where $e^{-G_{\mathrm{oh},i}/k_{\mathrm{B}}T} = e^{-G_{\mathrm{hyb},i}/k_{\mathrm{B}}T} + e^{-G_{\mathrm{dis},i}/k_{\mathrm{B}}T}$. The $G_{\mathrm{hyb},i}(\theta)$ and $G_{\mathrm{dis},i}(\theta)$ profiles plotted in Figure 3A inset exhibit opposite trends with respect to θ, namely, $G_{\mathrm{hyb},i}(\theta)$ becomes more favorable with decreasing angle due to increased stabilization of base-pairing interactions while $G_{\mathrm{dis},i}(\theta)$ becomes less favorable due to entropy loss, and both profiles rise sharply at small angles due to strand compression. Apart from echoing these results gleaned from the $G_{\mathrm{oh},i}(\theta, \xi)$ map, the $G_{\mathrm{hyb},i}(\theta)$ and $G_{\mathrm{dis},i}(\theta)$ profiles importantly also illustrate the sharp nature of the transition from dissociated to hybridized states as the hinge angle is decreased and its role in producing the energy barrier in the landscape. In particular, the two profiles intersect at an angle (say θ_{p}) that coincides with the location of the *peak* of the barrier, with hybridized states dominating the landscape at smaller angles and dissociated states dominating at larger angles. This is noted from $G_{\mathrm{hyb},i}(\theta)$ and $G_{\mathrm{dis},i}(\theta)$ profiles virtually tracing out the $G_{\mathrm{oh},i}(\theta)$ landscape in the $\theta < \theta_{\mathrm{p}}$ and $\theta > \theta_{\mathrm{p}}$ regions. The narrowness of the angle space about the barrier peak where *both* the hybridized and dissociated states contribute substantially to the overhang free energy landscape illustrates the sharp nature of this transition with respect to the hinge angle typical of a first-order transition.

Based on these results, the free energy landscape may be divided into the four 'zones' as depicted in Figure 3A: (i) *Steric repulsion* zone, where the overhangs are severely compressed between the hinge arms, resulting in large steric and electrostatic repulsion that prevents duplex formation but allows intermittent base-pairing interactions. (ii) *Hybridization* zone, where the separation distance between the overhang attachment points and the free volume between the hinge arms is in the range for the overhangs to form a stable duplex. (iii) *Dissociation* zone, where the separation distance goes beyond this ideal range for strand hybridization, causing the overhangs to prefer the dissociated state even though they continue to collide within the confined space and feel some steric and electrostatic repulsion from each other. (iv) *Non-interaction* zone, where the separation distance is so large that the strands do not interact with each other and exhibit dynamics independent of each other.

Effects of overhang position and cation concentration

The free energy landscape $G_{\mathrm{oh},i}(\theta)$ of overhang pairs corresponding to 10 distinct connection points (C1–C10) at 3 ion concentrations ($[Na^+] = 0.2$, 0.4 and 1.2 M) are collectively shown in Figures 4A–C; the free energy contributions $G_{\mathrm{oh},i}(\theta, \xi)$ from the various overhang hybridization states for each of these free energy landscapes are provided in Supplementary Figure S7. Most of the landscapes exhibit the characteristic features of a plateau, a barrier and a sharp minimum at large, intermediate, and small hinge angles discussed earlier. However, some of the landscapes, namely those computed at low $[Na^+]$ for overhangs attached far from the hinge vertex (C6–C10 at 0.2 M, and C9 and C10 at 0.4 M), do not display the minimum or the complete barrier. For these systems, the minimum is either missing or appears at very small angles where overhang conformations were challenging to sample in simulations.

More importantly, the landscapes display considerable differences between overhangs attached at the different connection points. In particular, the heights of the energy barriers at all three ionic conditions were found to decrease with increasing separation distance between the overhangs and the hinge vertex, that is, going from C1 to C10. Furthermore, the onset of the energy barrier and its width in angular terms both decrease with increasing distance of the overhangs from the vertex. This effect is largely geometric in nature, as overhangs distant from the vertex require smaller angles to come into close proximity to interact compared to those attached near the vertex. Hence, a more informative coordinate for revealing differences in interactions between overhang pairs connected at different distances from the vertex is the Euclidean distance d between the pair of connection points on the arms, which we term 'end-to-end distance' and calculate as $d = 2l \sin(\theta/2)$, where l is the distance of the connection points from the vertex. Indeed, when the landscapes of C1 through C10 are plotted in terms of their end-to-end distances (Figures 4D–F), the barrier onset and width become more similar across all overhangs. However, these 'normalized' landscapes now exhibit the opposite trend whereby the barrier onset and width *increases* with increasing distance of the overhang attachment point from the vertex, suggesting the intriguing proposition that overhang pairs attached far from the vertex exhibit longer-ranged interactions compared to those close to the vertex. The free energy landscapes also exhibit different sensitivities to changes in ion concentration depending on the attachment position of the overhangs, which are better visualized in Figure 4D–F. While the energy landscapes for overhangs attached close to the hinge vertex C1 to C3 are negligibly affected by changes in ion concentration, those for the more distant overhangs C4 through C10 show an increase in free energy gain from strand hybridization at small hinge angle with increasing ion concentration.

To investigate the origin of these attachment position-dependent differences in the free energy landscapes of the overhangs, we picked for further analysis two extreme locations of the overhangs, namely positions C1 and C10 clos-

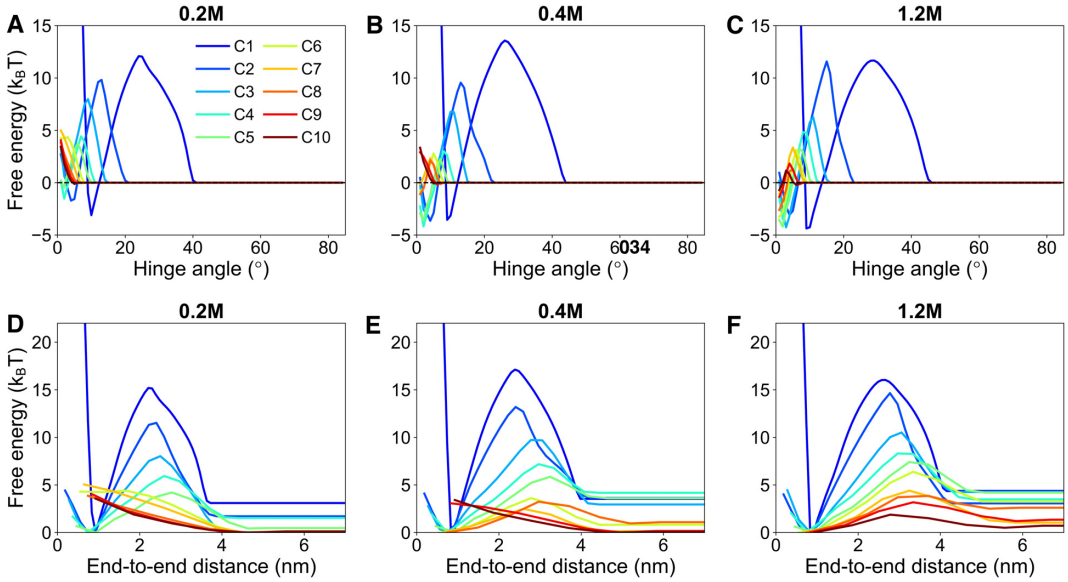

Figure 4. Effects of attachment location and salt concentration on the overhang free energy landscape. (A–C) Free energies $G_{oh,i}(\theta)$ plotted as a function of hinge angle for a pair of overhangs with 4 complementary bases attached at the various possible attachment sites (C1 through C10) computed at three different cation concentrations: (**A**) $[Na^+] = 0.2$ M, (**B**) $[Na^+] = 0.4$ M and (**C**) $[Na^+] = 1.2$ M. (**D–F**) Same free energies plotted instead as a function of the separation distance between the two attachment sites of the overhangs. The free energy curves are vertically shifted based on their minimum value for clarity.

est and farthest from the vertex. The C1 overhang exhibits the narrowest and largest energy barrier and low sensitivity to ionic conditions, whereas the C10 overhang exhibits the broadest and lowest barrier and highest ion sensitivity. Using the procedure described earlier, we decomposed the overall free energy of the two overhangs obtained at two ionic concentrations (0.2 and 1.2 M) into contributions $G_{hyb,i}$ arising from the subensemble of partly- to fully-hybridized states and $G_{dis,i}$ arising from dissociated overhangs (Figure 5A and B). We also carried out simulations of a single overhang attached to a repulsion plane (without the opposite overhang and repulsion plane), and analyzed the resulting conformational ensemble of the overhang. The results are plotted as a probability density map of the positions of the overhang bases projected onto a plane normal to the repulsion plane (bottom panel of Figure 5D).

The significantly larger energy barrier to hybridization displayed by the C1 overhang pairs compared to the C10 overhangs obviously stems from the much sharper rise in $G_{dis,i}(d)$ of C1 overhangs with decreasing distance d between repulsion planes as compared to C10 overhangs (*cf.* red dotted curves in Figure 5A and B). As discussed earlier, this rise in $G_{dis,i}$ is related to the entropic penalty of squeezing the overhangs in their fully dissociated state. This implies that the C1 overhang pair that interact within the confinement imposed by tilted repulsion planes incur much larger entropic penalty than the C10 overhangs, which interact within near-parallel planes. To explain this difference in entropy, we turn to the conformational behavior of a surface-tethered overhang strand provided in the bottom panel of Figure 5D. We observe that the overhang bases reside mostly within a narrow and short conical region about the attachment point, and the base probability density decays sharply to zero outside this region. Consider now the overlap between two such conical distributions representing interactions between a pair of surface-tethered overhangs over an 'intermediate' distance (e.g. $d \sim 3$ nm) where strands interact with each other but cannot form stable base pairs. When the repulsion planes are tilted relative to each other, corresponding to the C1 overhangs, their conical distributions are both pushed towards one side, implying that the two overhangs are highly likely to 'bump' into each other, explaining the large loss in their conformational entropy (Figure 5A, left cartoon). In contrast, parallel planes corresponding to the C10 overhangs give the strands the best chance to 'avoid' each other, and hence this configuration leads to small entropic losses (Figure 5B, left cartoon).

The earlier onset of the barrier of the C10 overhangs (4.5–6 nm for the three ionic conditions) compared to C1 overhangs (3.5–4 nm), which also leads to differences in their barrier widths, may also be explained using their conformational behavior. As discussed above, the two conical density distributions point head-on towards each other in the parallel-plane geometry exhibited by the C10 overhangs (Figure 5B, right cartoon), whereas the distributions approach each other at an angle in the tilted-plane geometry of the C1 overhangs (Figure 5A, right cartoon). At the large separation distances relevant here (e.g. $d \sim 5$ nm), both sets of conical distributions appear to exhibit similar overlaps. However, the C10 distributions overlap with their higher probability-density regions, which results in some entropy loss, whereas the C1 distributions overlap with their low probability-density regions, which sacrifices negligible entropy. Thus, the $G_{dis,i}(d)$ profiles for the C10 overhangs begin to rise at large distance as compared to C1 overhangs.

The free energy contributions shown in Figures 5A, B also reveal that the primary source of the difference in the sensitivity of the C1 and C10 overhangs to ionic condi-

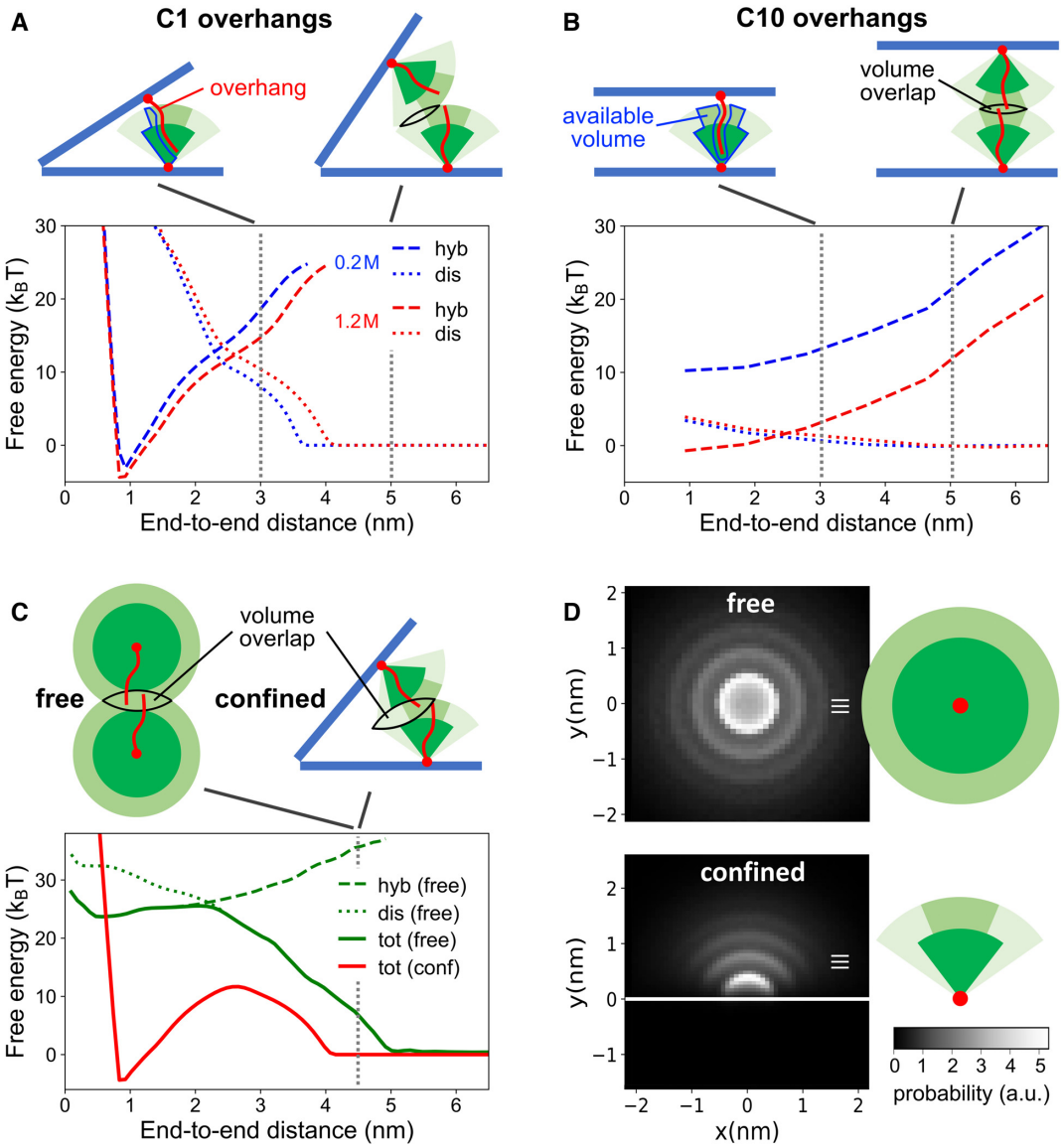

Figure 5. Effects of ion concentration and hinge confinement on the free energy landscape of the overhangs. (**A**) Comparison of free energy contributions from hybridized (dashed lines) and dissociated states (dotted lines) at $[Na^+] = 0.2$ M (blue) and 1.2 M (red) for C1 overhangs. (**B**) Same comparison carried out for the C10 overhangs. (**C**) Free energy landscape of *free* overhangs at $[Na^+] = 1.2$ M (solid green lines) along with contributions from hybridized and dissociated states overhangs (dashed and dotted green lines). The free energy landscape for confined C1 overhangs at the same ion concentration is shown for reference (solid red lines). (**D**) Probability distribution in the position of nucleotide bases for free overhangs (top) and overhangs confined by repulsion plane (bottom) along with cartoon representations of the probability distributions used in (A)–(C) to illustrate differences in the frequency of interactions between overhangs and or their ability to avoid each other (see text). Increasing brightness in the distribution maps and increasing color intensity in cartoons indicate increasing probability.

tions is the free energy of partly- to fully-hybridized states. Specifically, the $G_{hyb,i}$ curve for the C10 overhangs shifts downwards by $\sim 10 k_B T$ when $[Na^+]$ is increased from 0.2 to 1.2 M, consistent with the increased stabilization of the hybridized states of the overhangs due to increased electrostatic screening of their charged phosphate backbones. However, the corresponding $G_{hyb,i}$ curve for the C1 overhangs exhibits a much smaller shift, indicating that the tilted orientation of the repulsion planes somehow makes strand hybridization less sensitive to salt concentration. While the origin of this effect is not fully understood, it is likely related to the stronger confinement imposed by the tilted planes that limits the conformational space available to the overhangs, as explained above. In this regime dominated by steric interactions, the effects of salt concentration become less important, leading to smaller variations in $G_{hyb,i}$ with changing $[Na^+]$. As expected, the dissociated-state free energy curves $G_{dis,i}$ of *both* C1 and C10 overhangs remain largely unaffected by changes in ionic concentration, given that dissociated overhangs by definition remain physically separated from each other and therefore exhibit weak electrostatic interactions.

Lastly, we examined how the free energy landscapes of the *confined* overhangs shown in Figure 4 compare against

those of *free* overhangs in solution (without repulsion planes). Figure 5C presents such a comparison for a pair of free overhangs at 1.2 M Na^+ against the confined C1 overhangs at the same salt concentration. Since a hinge angle cannot be defined for free strands, all landscapes are plotted with respect to the end-to-end distance. Interestingly, the free overhangs exhibit a larger energy barrier than the confined overhangs, even the most confined ones (C1), and also do not exhibit a globally stable hybridized state unlike the confined strands. This is evidently due to the larger entropy loss incurred by the free strands when they hybridize compared to confined strands whose conformational freedom is already quite constrained as a result of the repulsion planes. Thus, for the free strands, the free energy gained by strand hybridization is insufficient to overcome the large entropy loss, resulting in a metastable hybridized state at 0.5 nm end-to-end distance. In addition, the free strands exhibit a broad energy barrier comparable to that of the C10 overhangs, but wider than that of the C1 overhangs. This observation may be explained using the same effect used earlier to explain the broader barrier displayed by the C10 strands *versus* the C1 strands. In other words, the spherically symmetric density distribution of the opposing free strands (Figure 5D, top panel) point head-on towards each other similar to the conical distributions of the C10 strands (Figure 5C, left cartoon), which implies that the two free strands 'feel' each other earlier than the C1 overhangs which approach each other at an angle (Figure 5C, right cartoon).

Effects of overhang length and sequence

Apart from overhang attachment position (relative to hinge vertex) and salt concentration, the sequence design of the overhangs is also expected to affect their free energy landscape. We have so far examined 7-base long overhangs with 4-base 'sticky' ends (GTCG and complement CGAC) and 3-base linkers (TTT); we denote this design by '4b3T'. To explore the effects of overhang sequence and gain deeper understanding of strand hybridization under confinement, we examined three *additional* designs, namely, overhangs with (i) longer, 6-base sticky ends of complementary sequences GTCGGC and GCCGAC, but unchanged linkers, which we denote by '6b3T'; (ii) longer, 5-base linkers (of sequence TTTTT) but unchanged sticky ends denoted by '4b5T'; and (iii) longer sticky ends *and* linkers of the above sequences denoted by '6b5T'.

Figures 6A–C compares the free energy landscapes of the four overhang designs for three different attachment positions (C2, C5 and C10). Our results show that changing the lengths of the linkers and the sticky ends both have strong effects on the landscape. Increasing the linker length from 3 to 5 bases, while keeping the sticky end unchanged, leads to higher and broader energy barriers and a shallower energy minimum. Both effects are nicely captured in Figure 6D, which shows a zoomed view of the landscapes of the 4b3T and 4b5T overhangs (attached at position C2) along with free energy contributions $G_{\mathrm{hyb},i}$ and $G_{\mathrm{dis},i}$ arising from their hybridized and dissociated states. The broader and higher barrier exhibited by the 4b5T overhangs is directly related to their longer *overall* length as compared to the 4b3T overhangs. Thus, the 4b5T overhangs begin to interact with each other at larger hinge angles, explaining the earlier onset of their barrier, and they also incur larger entropic penalty than the 4b3T overhangs at similar levels of confinement (hinge angles), explaining the higher barrier and lower stability of the hybridized state.

Increasing the length of the sticky end from 4 to 6 bases, keeping linker length unchanged, leads to significantly deeper energy minima, and generally slightly higher and wider barriers (see Figure 6E comparing the landscapes of 4b3T and 6b3T overhangs at position C2). The deeper minimum displayed by the 6b3T overhangs obviously arises from their longer sticky ends which exhibit stronger hybridization; their higher and wider barrier is again related to their longer overall length compared to 4bT3 overhangs, as discussed above.

Lastly, increasing the lengths of *both* the linker and the sticky end, i.e. in going from 4bT3 to 6bT5, leads to a combination of the two sets of effects discussed above, which we again demonstrate using the example of the C2-attached overhangs (Figure 6F). First, we observe that the depth of the energy minimum for the 6bT5 overhangs is intermediate to that of the 4bT3 and 6bT3 overhangs discussed earlier. While the sticky ends in the 6bT5 and 6bT3 overhangs are identical, the former are overall longer, which leads to stronger entropic repulsion and thereby less favorable hybridization. Second, based on their longer overall length, the 6bT5 overhangs exhibit higher and wider energy barriers than both 4bT5 and 6bT3 overhangs. The longer length also implies that the location of the energy minimum for the 6bT5 overhangs is the most shifted to wider hinge angles. Interestingly, the free energy landscapes for the 4bT5 and 6bT3 overhangs with different linkers and stick ends *but* identical overall lengths exhibit similar locations of their minima.

The above results thus demonstrate that the lengths of the linker and sticky portions of the overhangs both affect the stability of the hybridized state of the overhangs and the height and width of the energy barrier. In general, long sticky ends with short linkers will prefer the fully hybridized state (e.g. 6b3T overhangs) and short sticky ends with long linkers will prefer to stay dissociated (e.g. 4b5T overhangs).

Bare hinge and overall free energy landscapes

Having thoroughly studied the free energies $G_{\mathrm{oh},i}(\theta)$ of individual overhangs, we next investigated the free energy landscape $G_{\mathrm{bh}}(\theta)$ of the bare hinge and the free energy landscape $G_{\mathrm{hinge}}(\theta)$ of the full hinge complete with *all* the overhangs. The computed free energy landscape of the bare hinge is shown in Figure 7A. The landscape exhibits a largely parabolic shape with a minimum at 80°, which matches very well with the equilibrium hinge angle measured experimentally (22). However, the energy landscape rises much more steeply compared to that inferred from the experimental hinge-angle distribution (Figure 7A and Supplementary Figure S8). This difference could arise due to various factors not accounted in our model, including hinge deformations, structural defects, and ionic and solvation effects, that might relieve the stresses associated with closing the hinge arms. Hence, we chose to use the bare-hinge landscape de-

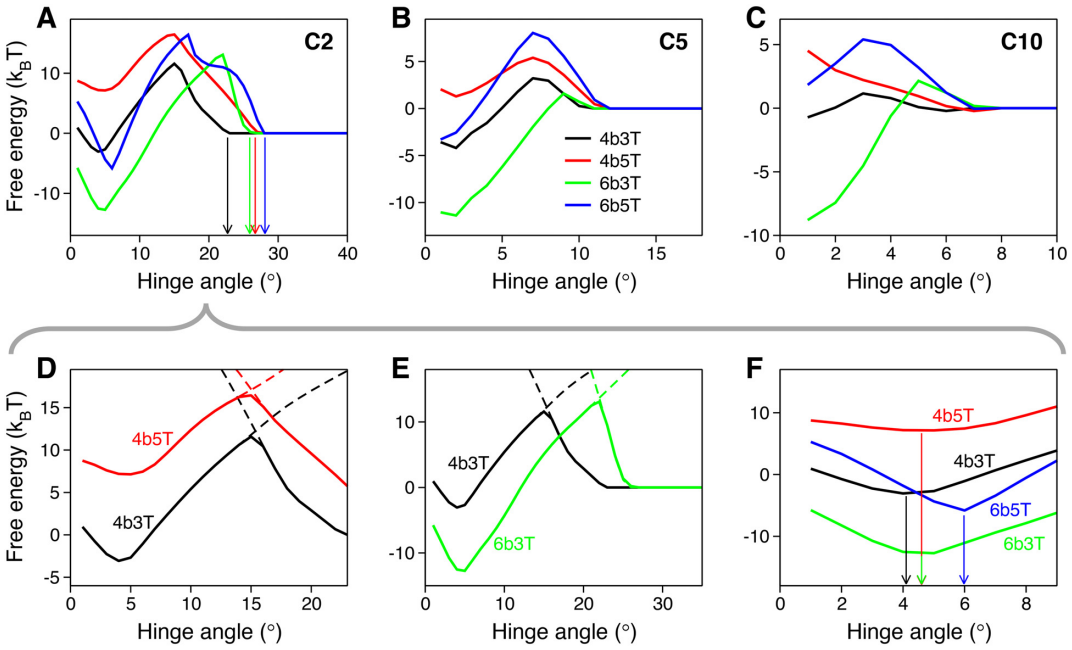

Figure 6. Effects of the lengths of the sticky and linker portions of the overhangs on their free energy landscape. (A–C) Free energy landscape of overhangs attached at positions C2 (**A**), C5 (**B**) and C10 (**C**) on hinge arms for overhangs with 4–6 base sticky regions and 3–5 base linker regions: 4b3T (black lines), 4b5T (red), 6b3T (green) and 6b5T overhangs (blue). (D, E) Zoomed portions of the energy landscape of the C2 overhangs used for illustrating specific effects discussed in the text. Dashed lines in (**D**) and (**E**) denote contributions to landscape from hybridized and dissociated states of the overhangs. Arrows in (A) and (**F**) help clarify differences in the locations of the barrier onset and minimum for the four types of overhangs.

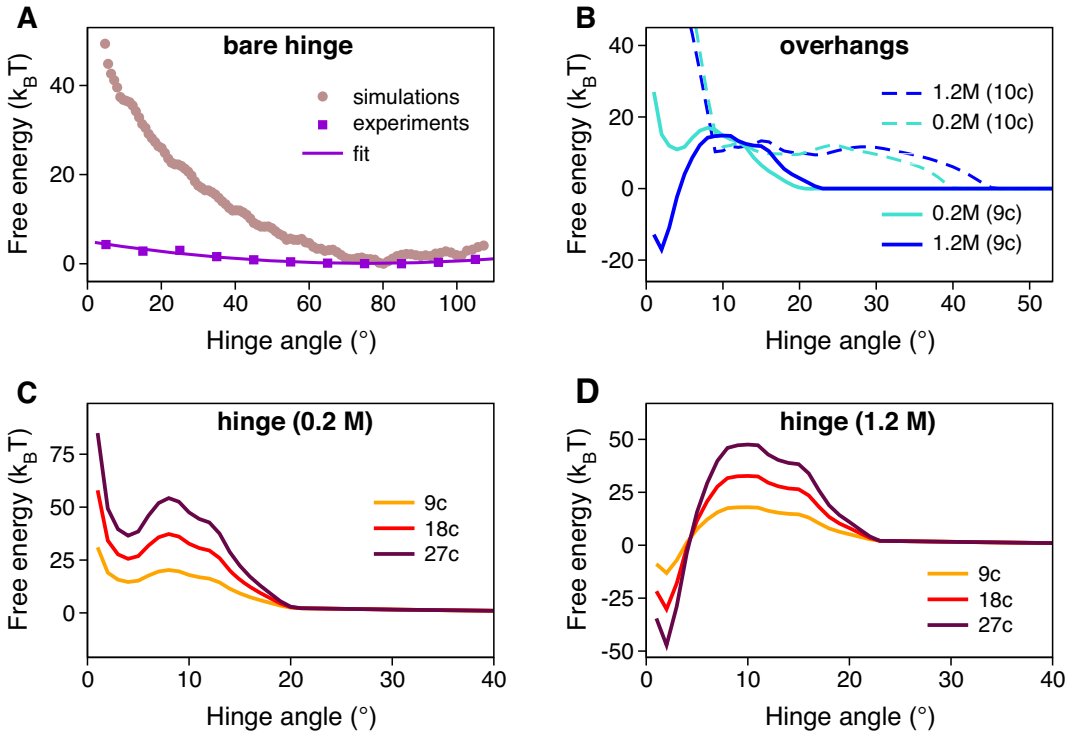

Figure 7. Overall free energy landscape of the hinge and contributions from the bare hinge and the overhangs. (**A**) Computed free energy landscape of the bare hinge (brown symbols), and the landscape inferred from experiments (violet symbols) along with its harmonic fit (violet line). (**B**) Cumulative free energy landscape at $[Na^+] = 0.2$ M (cyan lines) and 1.2 M (blue lines) from one overhang attached at each of the 10 positions C1 through C10 (dashed lines) and from nine overhangs attached at each of those positions except C1 (solid lines). (C, D) Overall hinge free energy landscapes obtained at $[Na^+] = 0.2$ M (**C**) and 1.2 M (**D**) for hinges with one (orange), two (red) and three overhangs (brown) attached at each of the nine positions C2 through C10.

rived from experiments to keep all subsequent analyses as realistic as possible.

The experiments studied hinges with 10, 20 and 30 overhang connections corresponding to one, two, and three pairs of overhangs located at each of the positions C1 through C10 on the hinge arms (see Figure 1A). Consistent with these experiments, we attempted to compute the cumulative free energy $G_{\rm oh}(\theta) \equiv \sum_i G_{{\rm oh},i}(\theta)$ contributed by 10, 20 and 30 pairs of overhangs. However, we found that the overhang pair attached at C1 closest to the vertex contributed excessively large steric repulsion for angles smaller than 10° (Figure 7B, dashed lines), essentially preventing the hinge from closing its arms even at the highest salt concentration considered here. This is not consistent with experiments which clearly show hinges in the closed state exhibiting near-zero bending angles. We therefore speculate that the experimental hinges did not properly incorporate these overhangs close to the vertex or that the hinge joint expanded slightly to mitigate the steric repulsion arising from the strongly squeezed C1 overhangs, an effect that is not accounted for by our planar and impenetrable repulsion planes. In addition, the interhelix spacing tends to open up in between crossover junctions, which can provide some room for the overhangs to occupy and reduce steric repulsion. Thus, for all remaining analyses, we considered only the overhangs attached at locations C2 through C10, that is, examining hinges with 9, 18 and 27 overhang connections.

Figure 7C and D presents the overall free energy landscape of the hinges with 9, 18, and 27 connections at low and high salt concentrations (0.2 and 1.2 M), obtained by summing up contributions from the bare hinge and each overhang pair. Our results reveal that all three hinges strongly prefer to remain open at $[Na^+] = 0.2$ M, and their closed conformation appears only as a metastable state. In addition, the relative stability of the open state (with respect to the closed state) increases from ∼15 to 36 $k_{\rm B}T$ as the number of connections increases from 9 to 27. In contrast, the hinges strongly prefer the closed state at high salt concentration of 1.2 M. The relative stability of the closed state increases from roughly 13 to 45 $k_{\rm B}T$ with increasing number of connections. Interestingly, the open and closed states are separated by a fairly broad energy barrier (spanning >20°) whose height also rises with increasing number of connections (from ∼18 to 47 $k_{\rm B}T$). The generally broad and flat shape of this barrier largely arises from the superposition of barriers contributed by individual overhangs, which are much narrower and offset from each other. These results thus demonstrate how changes in salt concentration could be used to drive the hinges from the open to the closed conformation, and *vice versa*, how changing the number of the connections can be used to sharpen the relative stabilities of the open and closed states and modulate the height of the barrier separating the two states.

The hinges explored above considered a fixed distribution of overhang positions, namely, equal number of overhangs at each of the attachment sites C1–C10. However, this distribution could also be used as a variable to tune the actuation response of the hinges, given the sensitivity of overhang free energy landscapes to attachment positions (Figure 4). For instance, overhangs attached *very close* to the hinge vertex (e.g. at position C1) facilitate early closing of the hinge, i.e. at large angles, but due to strong steric repulsion, such overhangs cannot fully close the hinge arms. Furthermore, these overhangs introduce a large barrier to hinge closing, and a free energy of hybridization that is favorable at both weak and strong ionic conditions. This suggests that hinges containing only these overhangs will stay partially open, irrespective of ionic conditions, and will thus be unable to undergo salt-mediated actuation. In contrast, overhangs attached at *intermediate* distances (e.g. at positions C2 to C5) should allow the hinge arms to close fully. With increasing distance from the vertex, these overhangs present increasingly smaller barriers and smaller angles for initiating the hinge-closing transition. While these overhangs also display a propensity to stably hybridize under weak and strong ionic conditions, they do so with lower stability at low ionic concentrations. This implies that with a sufficiently large barrier to hinge closing contributed by the bare-hinge landscape, these overhangs should be able to support reversible actuation of hinges via changes in salt conditions. Lastly, overhangs attached *far* from the vertex (e.g. at positions C6 to C10) not only present small energy barriers but also the hybridization thermodynamics necessary for reversible salt-mediated actuation, that is, stable hybridized state at high ion concentration and stable dissociated state at low concentration. However, these overhangs on their own would introduce a narrow energy barrier that does not provide sufficient angular distinction between the open and closed states; in other words, the open hinge state would still allow very small angles to be sampled. Thus, a wide distribution of overhangs spanning distances both proximal and distal from the vertex (but not too proximal like the C1 overhangs) would help produce a broad energy barrier for stronger separation of the open and closed hinge states. Such distribution of overhangs will importantly also prevent accumulation of large energy barriers that might result from colocalization of individual energy barriers contributed by overhangs attached at similar distances from the vertex. Interestingly, our experiments inadvertently used such a distribution strategy to achieve rapid actuation of hinges with millisecond time scales (22).

DISCUSSION

We used molecular simulations to investigate the free energy landscape of reconfigurable DNA origami hinges, specifically to elucidate how collective hybridization and dehybridization of short, single-stranded DNA connections between hinge arms triggered by changes in salt concentration could be used to actuate the hinges between open and closed conformations. To tackle this computationally challenging problem, we devised a strategy where the overall free energy of the hinge was decomposed into contributions arising from the bare hinge and from the individual DNA overhangs attached at different locations on the arms. The two contributions were then separately computed using efficient methods tailored for sampling global hinge motions and local base-pairing interactions, enabling the free energy landscape of the hinges to be determined within reasonable computational costs. Such breakdown of free energies also helped us gain crucial insights into the roles of individual hinge components in dictating the overall actua-

tion response of the hinges. From a broader perspective, this strategy could enable challenging free-energy calculations on other large DNA structures and biomolecular complexes such as proteins involving large, rigid components with fast relaxation times and small, associating elements with slow relaxation times.

Our calculations revealed the free energy landscape of individual overhang pairs attached on the hinge arms, providing one of the first detailed picture of DNA hybridization under angular confinement. The landscapes were found to exhibit a sharp minimum at small angles and a broad barrier at intermediate angles that are respectively flanked by a steep repulsive wall at smaller angles and a plateau at larger angles. We analyzed the molecular origins of these features, revealing that: the energy barrier arises from the combined effect of the unhybridized configurations of the overhangs incurring confinement-induced entropy loss and electrostatic repulsion, and the partly and fully-hybridized configurations undergoing distortion to form base pairs; the energy minimum arises from the increased stabilization of the hybridized state brought about by confinement that more than compensates the accompanying entropy loss and electrostatic repulsion; and the repulsive wall arises from steric compression of the overhangs. Interestingly, the tilted confinement imposed by the hinge arms was found to stabilize the hybridized state of the overhangs, which preferred to stay dissociated in the absence of confinement. We showed how free strands incur much larger entropic penalties to hybridization as compared to confined ones whose conformational freedom is already quite restricted due to the hinge arms at large hinge angles. Our results thus reveal a fundamental distinction between DNA hybridization under angular confinement *versus* that in solution. These findings on confined hybridization of end-tethered DNA strands extends beyond the case of salt-mediated actuation; for instance, such a scenario appears during DNA-mediated assembly of faceted nanoparticles into crystals where the surfaces of particles are brought into close proximity at parallel or tilted angles through hybridization of surface-tethered DNA strands (33).

We also studied in detail how the overhang landscapes were impacted by their length and attachment position, and salt concentration. As expected, longer sticky domains in the overhangs led to deeper minima, or stronger hybridization. Overall longer overhangs, irrespective of whether the length is added to the sticky or linker portions, led to higher energy barriers, which was explained in terms of the increased confinement entropy loss incurred by the longer strands. Placing the overhangs farther from the vertex resulted in lower energy barriers, which are also wider when the free energy was plotted as a function of the distance between the complementary overhang attachment sites but narrower when plotted in terms of hinge angle. The first two effects are not so obvious. These were rationalized based on how surface-tethered overhangs exhibit a cone-shaped conformational distribution and how differently two such distributions interact with each other for overhangs attached at different distances from the hinge vertex. The last effect is obviously geometric given that a distant overhang requires smaller changes in hinge angle to traverse the same distance as an overhang attached proximally to the vertex. Lastly, salt concentration seemed to only predominantly affect the landscapes of distal overhangs, causing increased stabilization of the hybridized states with increasing concentration as would be expected from electrostatic screening effects. The landscapes of proximal overhangs were negligibly affected, which we attributed to the dominance of steric effects in such overhangs. Our results thus suggest that: the hybridization strength of the overhangs is best tuned by the length of their sticky ends; the barrier to hybridization is best tuned by the attachment position or length of the linker regions of overhangs, and salt-mediated actuation is best carried out by overhangs distal from the vertex.

Finally, we analyzed the overall free energy landscape of the full hinge obtained by combining the landscapes computed for all overhangs and the bare hinge. Such a landscape holds crucial information about the actuation behavior of the hinges: First, the salt dependence of the free energy difference $\Delta G_{\text{c-o}}([\text{Na}^+])$ between the closed (c) and open (o) states dictates the actuation response $P_{\text{c}}([\text{Na}^+])$ of the hinges via $P_{\text{c}} \simeq \exp(-\Delta G_{\text{c-o}}/k_{\text{B}}T)/[1 + \exp(-\Delta G_{\text{c-o}}/k_{\text{B}}T)]$, where $P_{\text{c}}([\text{Na}^+])$ is the equilibrium probability of observing the closed state. Second, the shape of the energy landscape governs the kinetics of actuation; for instance, based on Kramers theory (39,40), the rate constant k of the hinge-closing transition would be given by $k \simeq k_0 \exp(-\Delta G_{\text{b-o}}([\text{Na}^+])/k_{\text{B}}T)$, where $\Delta G_{\text{b-o}}$ is the height of the energy barrier (b) relative to the open state and k_0 is related to the solvent friction coefficient and the curvatures of the free energy minimum and barrier. We started by examining the landscapes of three experimentally-studied hinge designs containing different numbers of overhang connections distributed evenly across the hinge arms. The computed landscapes exhibited an energy minimum at the closed state and a broad energy barrier separating the closed and open states. The landscapes nicely captured the increasing propensity of the experimental hinges to remain open (at low salt) or closed (at high salt) with increasing number of connections. The landscapes further revealed proportional increase in the height of the barrier with the number of connections, suggesting that while simple scale-up of the number of connections helps sharpen the actuation response of the hinge, it could also lead to slower actuation kinetics. Next, we demonstrated how the actuation response and kinetics, related to features of the landscape, could be tuned by manipulating the positional distribution of the overhangs, enabling combinations of sharp or dull actuation responses with fast or slow kinetics to be achieved. This feature along with the ability to tune and predict individual energy landscapes contributed by each overhang pair should enable design of hinges with the desired responses and kinetics.

While our computations provided many useful insights and predictions on confined hybridization and salt-mediated actuation, several approximations in the approach may limit its accuracy and applicability. First, the oxDNA model used for modeling the hinge in our approach uses a Debye-Hückel approximation to treat electrostatic screening by ions. Hence, our approach is limited to studying actuation by monovalent ions such as Na^+, and not multivalent ions such as Mg^{2+} and Spd^{3+} that have more complex effects. Second, our previous work showed that DNA hinge joints allow for some secondary motions like slid-

ing and twisting, in addition to its primary bending motion. These additional modes, which could provide opportunities for the hinge arms to relieve strong steric repulsion from the overhangs at small hinge angles, are currently ignored in our free energy calculations, which assume a single reaction coordinate, the hinge angle. Third, the repulsion planes we used for enabling the otherwise computationally challenging overhang free energy calculations treat the hinge arms as rigid planes. In reality, the hinge arms display a corrugated surface, with gaps between DNA helices that become wider between crossover junctions, and the arms can also potentially undergo deformation during severe compression of the overhangs. As discussed earlier, both these effects could also help mitigate steric interactions between overhangs at small hinge angles. Fourth, the overall free energy landscapes presented in Figure 7C and D for hinges with 18 and 27 overhang pairs assumed that all copies of overhang pairs at positions C2–C10 exhibit identical free energies. However, this may not be true as part of these copies of overhangs may be attached at the outermost helices, where they will experience lesser confinement effects. Further work is required to address each of these effects and to improve upon these approximations to provide finer, more accurate descriptions of salt-mediated actuation.

CONCLUSION

We recently proposed a new approach for actuating DNA nanodevices that involves integrating short, complementary ssDNA overhangs to their structural elements, which can then be latched together or unlatched via collective hybridization or dehybridization of the overhangs triggered by changes in solution ionic conditions. In this study, we used molecular simulations and free energy calculations to establish the molecular-thermodynamic basis of this actuation approach, using DNA origami hinges as our model system. To enable calculation of free energies at reasonable costs, we decomposed the overall free energy of the hinge into contributions from the bare hinge and from each pair of overhang attached to the hinge arms, allowing each contribution to be computed separately in a tractable manner. The resulting free energy landscapes revealed the stable, metastable and transition states exhibited by the hinges, and also provided predictions on the relative stability of the open *versus* closed states of the hinges and of the height of energy barrier separating the two states. Our free energy decomposition strategy allowed us to dissect these features of the landscape in terms of contributions from the bare hinge and from each hybridizing pair of overhangs. By elucidating the dependence of the overhang free energy contributions on salt concentration, we were able to uncover the molecular origins of our salt-based actuation method. Furthermore, by elucidating the effects of the length, sequence, and attachment position of the overhangs, we were able to provide simple guidelines for designing and tuning the actuation behavior of the hinges. Lastly, we discovered a stabilizing role of confinement on the hybridization between tethered DNA strands, an effect that has applications beyond this actuation method. Together, these results provide a significantly deeper fundamental understanding of the mechanism behind a new, promising approach for reconfiguring nanodevices.

SUPPLEMENTARY DATA

Supplementary Data are available at NAR Online.

ACKNOWLEDGEMENTS

We thank Dr Carlos Castro and Dr Thomas Ouldridge for useful discussions.

FUNDING

National Science Foundation (NSF) [CMMI-1921955 to G.A.]; Computational resources were provided by the NSF XSEDE program [ACI-1053575]. Funding for open access charge: NSF [CMMI-1921955].
Conflict of interest statement. None declared.

REFERENCES

1. Bath,J. and Turberfield,A.J. (2007) DNA nanomachines. *Nat. Nanotechnol.*, **2**, 275–284.
2. Omabegho,T., Sha,R. and Seeman,N.C. (2009) A bipedal DNA Brownian motor with coordinated legs. *Science*, **324**, 67–71.
3. Pan,J., Li,F., Cha,T.-G., Chen,H. and Choi,J.H. (2015) Recent progress on DNA based walkers. *Curr. Opin. Biotechnol.*, **34**, 56–64.
4. Yan,H., Zhang,X., Shen,Z. and Seeman,N.C. (2002) A robust DNA mechanical device controlled by hybridization topology. *Nature*, **415**, 62–65.
5. Castro,C.E., Su,H.-J., Marras,A.E., Zhou,L. and Johnson,J. (2015) Mechanical design of DNA nanostructures. *Nanoscale*, **7**, 5913–5921.
6. Kuzyk,A., Schreiber,R., Zhang,H., Govorov,A.O., Liedl,T. and Liu,N. (2014) Reconfigurable 3D plasmonic metamolecules. *Nat. Mater.*, **13**, 862–866.
7. DeLuca,M., Shi,Z., Castro,C.E. and Arya,G. (2019) Dynamic DNA nanotechnology: toward functional nanoscale devices, *Nanoscale Horiz.*, doi:10.1039/C9NH00529C.
8. Kuzuya,A., Sakai,Y., Yamazaki,T., Xu,Y. and Komiyama,M. (2011) Nanomechanical DNA origami 'single-molecule beacons' directly imaged by atomic force microscopy. *Nat. Commun.*, **2**, 448–449.
9. Gu,H., Yang,W. and Seeman,N.C. (2010) DNA scissors device used to measure MutS binding to DNA mis-pairs. *J. Am. Chem. Soc.*, **132**, 4352–4357.
10. Ranallo,S., Prévost-Tremblay,C., Idili,A., Vallée-Bélisle,A. and Ricci,F. (2017) Antibody-powered nucleic acid release using a DNA-based nanomachine. *Nat. Commun.*, **8**, 15150.
11. Yurke,B., Turberfield,A.J., Mills,A.P., Simmel,F.C. and Neumann,J.L. (2000) A DNA-fuelled molecular machine made of DNA. *Nature*, **406**, 605–608.
12. Ketterer,P., Willner,E.M. and Dietz,H. (2016) Nanoscale rotary apparatus formed from tight-fitting 3D DNA components. *Sci. Adv.*, **2**, e1501209.
13. Gerling,T., Wagenbauer,K.F., Neuner,A.M. and Dietz,H. (2015) Dynamic DNA devices and assemblies formed by shape-complementary, non-base pairing 3D components. *Science*, **347**, 1446–1452.
14. Kamiya,Y. and Asanuma,H. (2014) Light-driven DNA nanomachine with a photoresponsive molecular engine. *Acc. Chem. Res.*, **47**, 1663–1672.
15. Kuzyk,A., Urban,M.J., Idili,A., Ricci,F. and Liu,N. (2017) Selective control of reconfigurable chiral plasmonic metamolecules. *Sci. Adv.*, **3**, e1602803.
16. Modi,S., Swetha,M.G., Goswami,D., Gupta,G.D., Mayor,S. and Krishnan,Y. (2009) A DNA nanomachine that maps spatial and temporal pH changes inside living cells. *Nat. Nanotechnol.*, **4**, 325–330.
17. Kopperger,E., List,J., Madhira,S., Rothfischer,F., Lamb,D.C. and Simmel,F.C. (2018) A self-assembled nanoscale robotic arm controlled by electric fields. *Science*, **359**, 296–301.

18. Lauback,S., Mattioli,K.R., Marras,A.E., Armstrong,M., Rudibaugh,T.P., Sooryakumar,R. and Castro,C.E. (2018) Real-time magnetic actuation of DNA nanodevices via modular integration with stiff micro-levers. *Nat. Commun.*, **9**, 1446.
19. Siavashpouri,M., Wachauf,C.H., Zakhary,M.J., Praetorius,F., Dietz,H. and Dogic,Z. (2017) Molecular engineering of chiral colloidal liquid crystals using DNA origami. *Nat. Mater.*, **16**, 849–856.
20. Bae,W., Kim,K., Min,D., Ryu,J.-K., Hyeon,C. and Yoon,T.-Y. (2014) Programmed folding of DNA origami structures through single-molecule force control. *Nat. Commun.*, **5**, 5654.
21. Li,L., Tian,X., Dong,Z., Liu,L., Tabata,O. and Li,W.J. (2013) Manipulation of DNA origami nanotubes in liquid using programmable tappingmode atomic force microscopy. *IET Micro Nano Lett.*, **8**, 641–645.
22. Marras,A.E., Shi,Z., Lindell,M.G., Patton,R.A., Huang,C.-M., Zhou,L., Su,H.-J., Arya,G. and Castro,C.E. (2018) Cation-activated avidity for rapid reconfiguration of DNA nanodevices. *ACS Nano*, **12**, 9484–9494.
23. Šulc,P., Romano,F., Ouldridge,T.E., Rovigatti,L., Doye,J.P.K. and Louis,A.A. (2012) Sequence-dependent thermodynamics of a coarse-grained DNA model. *J. Chem. Phys.*, **137**, 135101.
24. Ouldridge,T.E., Louis,A.A. and Doye,J.P.K. (2011) Structural, mechanical, and thermodynamic properties of a coarse-grained DNA model. *J. Chem. Phys.*, **134**, 085101.
25. Šulc,P., Ouldridge,T.E., Romano,F., Doye,J. P.K. and Louis,A.A. (2014) Simulating a burnt-bridges DNA motor with a coarse-grained DNA model. *Natural Comput.*, **13**, 535–547.
26. Matek,C., Ouldridge,T.E., Levy,A., Doye,J. P.K. and Louis,A.A. (2012) DNA cruciform arms nucleate through a correlated but asynchronous cooperative mechanism. *J. Phys. Chem. B*, **116**, 11616–11625.
27. Schreck,J.S., Ouldridge,T.E., Romano,F., Šulc,P., Shaw,L.P., Louis,A.A. and Doye,J.P. (2015) DNA hairpins destabilize duplexes primarily by promoting melting rather than by inhibiting hybridization. *Nucleic Acids Res.*, **43**, 6181–6190.
28. Romano,F., Hudson,A., Doye,J. P.K., Ouldridge,T.E. and Louis,A.A. (2012) The effect of topology on the structure and free energy landscape of DNA kissing complexes. *J. Chem. Phys.*, **136**, 215102.
29. Khara,D.C., Schreck,J.S., Tomov,T.E., Berger,Y., Ouldridge,T.E., Doye,J.P.K. and Nir,E. (2017) DNA bipedal motor walking dynamics: an experimental and theoretical study of the dependency on step size. *Nucleic Acids Res.*, **46**, 1553–1561.
30. Tee,S.R. and Wang,Z. (2017) How well can DNA rupture DNA? shearing and unzipping forces inside DNA nanostructures. *ACS Omega*, **3**, 292–301.
31. Shi,Z., Castro,C.E. and Arya,G. (2017) Conformational dynamics of mechanically compliant DNA nanostructures from coarse-grained molecular dynamics simulations. *ACS Nano*, **11**, 4617–4630.
32. Sharma,R., Schreck,J.S., Romano,F., Louis,A.A. and Doye,J.P.K. (2017) Characterizing the motion of jointed DNA nanostructures using a coarse-grained model. *ACS Nano*, **11**, 12426–12435.
33. Park,S.Y., Lytton-Jean,A.K., Lee,B., Weigand,S., Schatz,G.C. and Mirkin,C.A. (2008) DNA-programmable nanoparticle crystallization. *Nature*, **451**, 553–556.
34. Peterson,A.W., Heaton,R.J. and Georgiadis,R.M. (2001) The effect of surface probe density on DNA hybridization. *Nucleic Acids Res.*, **29**, 5163–5168.
35. Zhao,Z., Liu,Y. and Yan,H. (2011) Organizing DNA origami tiles into larger structures using preformed scaffold frames. *Nano Lett.*, **11**, 2997–3002.
36. Zero,K. and Pecora,R. (1982) Rotational and translational diffusion in semidilute solutions of rigid-rod macromolecules. *Macromolecules*, **15**, 87–93.
37. Broersma,S. (1960) Rotational diffusion constant of a cylindrical particle. *J. Chem. Phys.*, **32**, 1626–1631.
38. Meinkoth,J. and Wahl,G. (1984) Hybridization of nucleic acids immobilized on solid supports. *Anal. Biochem.*, **138**, 267–284.
39. Kramers,H.A. (1940) Brownian motion in a field of force and the diffusion model of chemical reactions. *Physica*, **7**, 284–304.
40. Arya,G. (2016) Models for recovering the energy landscape of conformational transitions from single-molecule pulling experiments. *Mol. Simulat.*, **42**, 1102–1115.